

Article

Heat Transfer Simulation and Structural Optimization of Spiral Fin-and-Tube Heat Exchanger

Huaquan Jiang ¹, Tingting Jiang ¹, Hongyang Tian ², Qiang Wu ², Congying Deng ^{2,*} and Renliang Zhang ³ 

¹ Chongqing Xiangguosi Gas Storage Limited Company, Chongqing 401121, China; jhq1007@petrochina.com.cn (H.J.); jiangtting@petrochina.com.cn (T.J.)

² School of Advanced Manufacturing Engineering, Chongqing University of Posts and Telecommunications, Chongqing 400065, China; t1409972827@163.com (H.T.); s242132022@stu.cqupt.edu.cn (Q.W.)

³ Chongqing Zhizhan Gear Transmission Co., Ltd., Chongqing 402260, China; zrl3417@163.com

* Correspondence: dengcy@cqupt.edu.cn

Abstract: The spiral fin-and-tube heat exchanger is a widely used heat transfer device in heating and cooling applications, and its performance is influenced by multiple structural parameters, including the pitch, thickness, and height of the fins, the diameter and thickness of the base tube, and the transverse and longitudinal tube spacings. This study comprehensively explores how these factors affect the heat transfer performance of the spiral fin-and-tube heat exchanger and aims to determine its optimal configuration of structural parameters. First, orthogonal experiments are arranged based on these factors to conduct the corresponding finite element numerical simulations and to determine the effects of these factors on the heat transfer and resistance performance of the spiral fin-and-tube heat exchanger. Subsequently, support vector regression (SVR) is introduced to predict the heat transfer factor and the resistance factor, with the aim of benefiting the construction of a multi-objective optimization model for optimizing the two factors simultaneously. Then, a comprehensive performance indicator is used to transform the multi-optimization problem to a single optimization problem, and the genetic algorithm is adopted to solve an optimal configuration of the heat exchanger structural parameters. Ultimately, the finite element numerical simulation is utilized to validate the accuracy of the optimization. Case studies are conducted on a specific spiral fin-and-tube heat exchanger. After the optimization, the heat transfer factor is improved by 44.44%, and the resistance factor is increased by 14.19%. However, the comprehensive performance indicator is increased by 38.79%.

Keywords: spiral fin-and-tube; heat transfer performance; multi-objective optimization; finite element numerical simulation; support vector regression



Citation: Jiang, H.; Jiang, T.; Tian, H.; Wu, Q.; Deng, C.; Zhang, R. Heat Transfer Simulation and Structural Optimization of Spiral Fin-and-Tube Heat Exchanger. *Electronics* **2024**, *13*, 4639. <https://doi.org/10.3390/electronics13234639>

Academic Editor: Domenico Mazzeo

Received: 19 September 2024

Revised: 13 November 2024

Accepted: 22 November 2024

Published: 25 November 2024



Copyright: © 2024 by the authors. Licensee MDPI, Basel, Switzerland. This article is an open access article distributed under the terms and conditions of the Creative Commons Attribution (CC BY) license (<https://creativecommons.org/licenses/by/4.0/>).

1. Introduction

Heat exchangers play a crucial role in industrial production and residential applications, covering cooling and heating processes ranging from power generation to metal-lurgy [1], such as the air conditioning, electronic manufacturing equipment, and petroleum refining. As the issue of global warming gradually becomes the focus, improving the efficiency of heat exchangers can not only save energy, but also reduce the pressure on the environment by reducing waste heat emissions. Researchers have improved the efficiency of heat exchangers through two aspects. On the one hand, they have optimized the structural design of equipment; on the other hand, they have formulated and improved empirical formulas to guide the design and application of heat exchangers.

Despite the relatively mature research on finned tube heat exchangers, much of the focus remains on the type selection and structural optimization of straight finned heat exchangers, while the spiral finned tube heat exchanger, which is widely used in the market, has received less attention [2]. However, the spiral finned heat exchanger is particularly important due to its unique advantages. Firstly, the spiral-structured fins

effectively increase the heat exchange area and promote complex fluid flow over the tube surface, significantly enhancing heat transfer efficiency. Secondly, the design of these spiral fins facilitates natural air circulation, effectively reducing the pressure drop on the air side and thus reducing energy consumption. In addition, the integrated design of the fins and pipes enhances the strength and pressure resistance of the overall structure. Finally, spiral finned heat exchangers are suitable for heat exchange between various fluids; this has led to their widespread adoption in multiple industrial and construction fields. These characteristics indicate that further research on optimizing spiral finned heat exchangers has significant potential application prospects.

Thermal resistance and heat transfer efficiency are key performance indicators when evaluating heat exchangers equipped with fins or other extended surfaces. The research has extensively explored improving the heat transfer efficiency by minimizing thermal resistance. Rich [3] explored the influence of geometric parameters on the performance of heat exchangers and experimentally studied the specific effects of fin spacing and tube row quantity on heat exchanger efficiency. Subsequently, researchers such as McQuiston [4], Gray [5], and Webb [5] further expanded their theoretical research based on this foundation. They established empirical formulas for predicting the relationship between the Colburn j factor and friction resistance f factor and the Reynolds number for straight fins in staggered tubes. The establishment of these empirical formulas provides a solid methodological foundation for the subsequent evaluation of the performance of finned tube heat exchangers.

In the study of the flow characteristics of spiral finned tube heat exchangers, researchers have focused on the influence of factors such as fin shape, pitch, height, thickness, and tube arrangement on flow and heat transfer performance. Through a series of experiments, Nuntaphan et al. [6] discovered that in spiral finned heat exchangers with an inline arrangement, an increase in fin height led to a significant rise in pressure loss, while the heat transfer coefficient decreased. In contrast, under a staggered arrangement, the device resistance was insensitive to changes in fin height and was primarily influenced by the tube pitch. Bhuiyan et al. [7] analyzed a four-row finned tube exchanger with 3D CFD technology and found that increasing the longitudinal and transverse spacing between tubes could reduce the heat transfer and friction coefficient in laminar and transitional flows. In both straight and staggered configurations, increasing the fin spacing increases these two coefficients. Meanwhile, the efficiency index increases with the increase in tube spacing and the decrease in fin spacing. Syuhada et al. [8] conducted a study on convective heat transfer in spiral finned tube heat exchangers with different fin spacing arrangements. The study showed that larger gaps result in less ideal turbulence effects and that excessively small gaps suppress the airflow rate. Keawkamrop et al. [9] conducted physical experiments to investigate the effects of segmented fin height and different fin spacing on air side performance. The fin height has a significant effect on the Nusselt number (Nu) and heat transfer factor, while the fin spacing plays a significant role in adjusting the friction factor and Euler number. Liu et al. [10] explored the flow and heat transfer characteristics of multi-waved internally spiral finned tubes through experiments and numerical studies and predicted the effects of inscribed circle diameter and spiral angle on the internal heat transfer performance of finned tubes. Afandi et al. [11] investigated the air-side heat transfer and pressure drop on compact heat exchangers with spiral finned tubes featuring sharp turns. The results showed that the smaller the spacing between fins, the higher the heat transfer rate, while the pressure drop increased as the pitch between fins decreased.

Mauro et al. [12] developed an optimization framework that adjusted foam porosity and pores per inch (PPI) using both mono- and multi-objective approaches. The mono-objective optimization maximizes thermal efficiency, while the multi-objective approach uses Pareto optimization to balance heat transfer and pressure drop. By controlling variables like PPI, porosity, and permeability with a local thermal nonequilibrium assumption, significant performance improvements were achieved with a high heat transfer coefficient

and optimal pressure drop. Bianco et al. [13] used a genetic algorithm to optimize a heat recovery ventilation (HRV) system with phase change materials (PCM) for thermal storage. Their model optimized tube diameter, thickness, and fan speed, enhancing efficiency from 37.5% to 44.4% while reducing costs and pressure drop. Rabienataj et al. [14] tackled the thermal conductivity limits of PCMs in electronic cooling by integrating fins to boost heat transfer. Using a feed-forward network and genetic algorithms, they optimized fin dimensions to reduce complete melting time (CMT). Single-objective optimization notably reduced CMT, while multi-objective optimization balanced cost and fin length, achieving a 192% CMT increase but cutting fin length by 286%.

In the research on optimizing the performance of heat exchangers, the methods involve selecting better heat exchanger materials and fluid materials, optimizing the structural parameters of heat exchangers, and improving the pipeline layout of heat exchangers. Park et al. [15] analyzed the fin angles, heights, lengths, and spacings of the offset strip fin heat exchangers, and presented a multi-objective optimization to enhance the heat transfer by 3.7% and reduce the pressure drop by 42.1% across six variables. Alavi et al. [16] evaluated the thermal performance of four airfoil turbulence generators with different thicknesses, pitch ratios, and Reynolds numbers by combining experimental and computational fluid dynamics methods. A genetic algorithm was used to optimize the objective function, which includes minimizing the friction factor and maximizing the Nusselt number, aiming to determine the Pareto front and find the optimal balance point between heat transfer efficiency and fluid resistance. Foruzan et al. [17] conducted research using computational fluid dynamics techniques, and the simulated annealing algorithm was introduced to evaluate the performance of the heat exchanger by single-objective optimization and multi-objective optimization. Lee et al. [18] proposed a new method for the topology optimization of heat exchangers using deep reinforcement learning (DRL), which improved the heat exchange efficiency by 14.8% compared to traditional optimization, demonstrating its effectiveness and practicality in complex engineering applications. Cao et al. [19] proposed a new design of internally finned helical coils and evaluated their heat transfer and flow resistance characteristics through numerical methods. In addition, they developed empirical formulas for calculating the Nusselt number and friction factor and presented an optimization method for optimizing the design of spiral coil heat exchangers.

Recent studies on spiral finned tubes have shown the growing interest among researchers regarding the enhancement of heat transfer efficiency and thermal performance through variations in fin configurations and design modifications. However, most of the existing designs of spiral finned tube bundles overlook the effects of internal fluid heat transfer, focusing primarily on external factors. Additionally, the explored structural parameters remain limited, lacking a comprehensive analysis of combined internal and external parameters. This research addresses these gaps by constructing a series of three-dimensional computational fluid dynamics (CFD) models for spiral finned tube bundles, analyzing parameters such as fin pitch, fin thickness, fin height, base tube diameter, base tube thickness, lateral spacing, and longitudinal spacing. Using an orthogonal experimental design, we systematically investigate the influence of each parameter on the heat exchanger's performance. To quantify heat transfer efficiency and resistance, we introduce the heat transfer factor j and the friction factor f , which are then combined into a comprehensive performance evaluation metric. Support vector regression (SVR) is employed to predict the j and f values, aiding in the development of an optimization model to balance these two factors. Finally, a genetic algorithm is utilized to determine the optimal structural configuration for the spiral finned tube bundles, with the optimized design parameters validated through finite element simulations to confirm their effectiveness. The finite element model stands as a pivotal component within the digital twin framework, furnishing potent tools for the analysis and assessment of heat exchanger performance across diverse operational scenarios. Moreover, by integrating surrogate modeling methodologies, it establishes a robust groundwork for refining the design of real-world heat exchangers, thereby

significantly augmenting the support extended to industries encompassing electronics, chemicals, and energy.

The rest of this paper is as follows. Section 2 introduces the variation range of each structural parameter of the finned tubes and presents an orthogonal experimental design for conducting the numerical simulations. In addition, this section also elaborates on the selection of computational unit models and the setting of their boundary conditions. Section 3 analyzes the specific effects of different parameters on the performance of heat exchangers based on the numerical simulations. Section 4 establishes a support vector regression model for predicting the performance indicators of the heat exchanger, and Section 5 uses a genetic algorithm to solve the optimization model and determine an optimal configuration of the heat exchanger structural parameters. The conclusion is provided in Section 6.

2. Materials and Methods

2.1. Physical Model Construction and Structural Parameter Design

The structure of the spiral finned tube bundle studied in this paper is shown in Figure 1. In order to investigate the influence of the structure of the heat exchanger and the arrangement of the tube bundles (transverse tube spacing and longitudinal tube spacing) on the heat transfer and resistance performance, a detailed range of parameter values for the finned tube bundle is listed in Table 1. This paper elaborated the value range table of the structural parameters of the tube bundles, as listed in Table 1. On this basis, according to the orthogonal experimental design scheme shown in Table 2, numerical simulation experiments were carried out on 49 groups of different parameter combinations. The variation ranges of the parameters in Table 1 are determined according to the studied heat exchanger provided by the enterprise and by referring to some of the references.

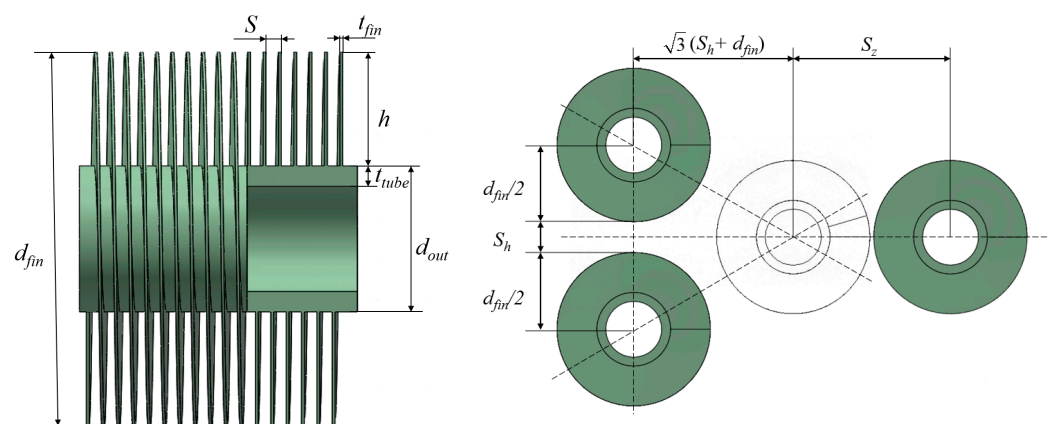


Figure 1. Helical finned tube and tube bundle arrangement.

Table 1. Value range of finned tube structure parameters.

| Factors | Levels | | | | |
|-----------------|--------|------|------|------|------|
| | 1 | 2 | 3 | 4 | 5 |
| S (mm) | 2.2 | 2.4 | 2.6 | 2.8 | 3 |
| t_{fin} (mm) | 0.3 | 0.4 | 0.5 | 0.6 | 0.7 |
| H (mm) | 13.5 | 15.5 | 17.5 | 19.5 | 21.5 |
| d_{out} (mm) | 25 | 26 | 27 | 28 | 29 |
| t_{tube} (mm) | 3 | 3.5 | 3 | 4.5 | 5 |
| S_h (mm) | 0.5 | 2.5 | 4.5 | 6.5 | 8.5 |
| S_z (mm) | 0 | 2 | 4 | 6 | 8 |

Table 2. Orthogonal table of finned tube structure parameters.

| Experiment Number | Factors | | | | | | |
|-------------------|----------|----------------|----------|----------------|-----------------|------------|------------|
| | S (mm) | t_{fin} (mm) | h (mm) | d_{out} (mm) | t_{tube} (mm) | S_h (mm) | S_z (mm) |
| 1 | 2.2 | 0.4 | 21.5 | 27 | 3.5 | 8.5 | 6 |
| 2 | 2.4 | 0.4 | 13.5 | 25 | 3 | 4.5 | 2 |
| 3 | 2.6 | 0.4 | 13.5 | 29 | 3 | 2.5 | 6 |
| 4 | 2.2 | 0.6 | 19.5 | 25 | 4 | 4.5 | 6 |
| 5 | 2.4 | 0.7 | 15.5 | 25 | 3 | 8.5 | 4 |
| 6 | 2.2 | 0.3 | 13.5 | 25 | 3 | 0.5 | 0 |
| 7 | 2.4 | 0.3 | 15.5 | 28 | 5 | 0.5 | 6 |
| 8 | 2.6 | 0.3 | 15.5 | 27 | 3.5 | 4.5 | 0 |
| 9 | 2.2 | 0.5 | 15.5 | 25 | 3.5 | 0.5 | 0 |
| 10 | 2.4 | 0.4 | 21.5 | 26 | 4.5 | 2.5 | 0 |
| 11 | 2.2 | 0.3 | 15.5 | 28 | 3 | 2.5 | 2 |
| 12 | 3 | 0.4 | 13.5 | 28 | 3.5 | 4.5 | 4 |
| 13 | 2.2 | 0.3 | 13.5 | 26 | 3.5 | 8.5 | 2 |
| 14 | 3 | 0.4 | 15.5 | 25 | 4.5 | 6.5 | 2 |
| 15 | 2.2 | 0.4 | 15.5 | 26 | 3 | 0.5 | 0 |
| 16 | 3 | 0.6 | 17.5 | 29 | 3 | 8.5 | 0 |
| 17 | 2.4 | 0.4 | 17.5 | 27 | 4 | 0.5 | 2 |
| 18 | 2.4 | 0.6 | 21.5 | 28 | 3.5 | 0.5 | 2 |
| 19 | 2.4 | 0.3 | 13.5 | 25 | 3.5 | 2.5 | 0 |
| 20 | 2.6 | 0.5 | 19.5 | 28 | 4.5 | 8.5 | 0 |
| 21 | 2.6 | 0.7 | 21.5 | 25 | 3 | 0.5 | 8 |
| 22 | 2.2 | 0.7 | 17.5 | 26 | 5 | 4.5 | 0 |
| 23 | 3 | 0.3 | 21.5 | 25 | 4 | 2.5 | 0 |
| 24 | 2.6 | 0.6 | 13.5 | 25 | 5 | 2.5 | 2 |
| 25 | 3 | 0.7 | 15.5 | 26 | 3.5 | 2.5 | 6 |
| 26 | 2.4 | 0.5 | 13.5 | 26 | 3 | 6.5 | 6 |
| 27 | 2.4 | 0.3 | 13.5 | 26 | 4 | 8.5 | 8 |
| 28 | 3 | 0.5 | 13.5 | 27 | 5 | 0.5 | 8 |
| 29 | 2.8 | 0.6 | 15.5 | 26 | 3.5 | 2.5 | 8 |
| 30 | 2.4 | 0.4 | 19.5 | 26 | 5 | 2.5 | 0 |
| 31 | 2.8 | 0.5 | 21.5 | 26 | 3 | 4.5 | 2 |
| 32 | 2.4 | 0.3 | 15.5 | 29 | 4.5 | 4.5 | 8 |
| 33 | 2.8 | 0.3 | 17.5 | 25 | 4.5 | 0.5 | 6 |
| 34 | 2.2 | 0.4 | 19.5 | 25 | 3.5 | 6.5 | 8 |
| 35 | 2.2 | 0.4 | 17.5 | 28 | 3 | 2.5 | 8 |
| 36 | 2.6 | 0.4 | 15.5 | 26 | 4 | 0.5 | 4 |
| 37 | 2.2 | 0.5 | 15.5 | 29 | 4 | 2.5 | 2 |
| 38 | 2.8 | 0.7 | 13.5 | 28 | 4 | 6.5 | 0 |
| 39 | 2.4 | 0.7 | 19.5 | 29 | 3.5 | 0.5 | 2 |
| 40 | 2.8 | 0.4 | 13.5 | 29 | 3.5 | 0.5 | 0 |
| 41 | 2.4 | 0.6 | 15.5 | 27 | 3 | 6.5 | 0 |
| 42 | 2.2 | 0.7 | 13.5 | 27 | 4.5 | 2.5 | 2 |
| 43 | 2.2 | 0.3 | 21.5 | 29 | 5 | 6.5 | 4 |
| 44 | 3 | 0.3 | 19.5 | 26 | 3 | 0.5 | 2 |
| 45 | 2.8 | 0.4 | 15.5 | 25 | 5 | 8.5 | 2 |
| 46 | 2.4 | 0.5 | 17.5 | 25 | 3.5 | 2.5 | 4 |
| 47 | 2.8 | 0.3 | 19.5 | 27 | 3 | 2.5 | 4 |
| 48 | 2.2 | 0.6 | 13.5 | 26 | 4.5 | 0.5 | 4 |
| 49 | 2.6 | 0.3 | 17.5 | 26 | 3.5 | 6.5 | 2 |

In this paper, the symbol S represents the fin pitch of the spiral fin tube, t_{fin} is used to indicate the thickness of the fin, h represents the height of the fin; t_{tube} indicates the thickness of the base tube, d_{out} is used to refer to the outside diameter of the base tube, and d_{fin} represents the outer diameter of the fin. S_h is the transverse spacing between the top fins of the two heat exchange tubes, and the longitudinal distance S_z is determined

by the length of the heat exchange tube from the original position to the far end in an equilateral arrangement.

The formula for calculating the length of a helical finned tube heat exchanger is:

$$L = nS + t_{fin} + 2 \tag{1}$$

where

L denotes the total length of the base tube (mm).

n represents the number of helical fin coils or fin turns along the tube.

The additional constant term “2 mm” accounts for the extra 1 mm extension at each end of the tube, which provides space for the base tube without fins.

When studying the convective heat transfer of the finned tube heat exchanger, this paper includes the wind speed of the external fluid as the 8th influencing factor and considers the influence of wind speed on heat transfer efficiency and pressure drop. In order to investigate the specific effects of wind speed on heat transfer performance and pressure drop performance, three different levels of wind speed values were set in the experiment, and the specific values are shown in Table 3.

Table 3. Value of wind speed.

| Levels | 1 | 2 | 3 |
|-----------|---|---|---|
| v (m/s) | 1 | 3 | 5 |

Therefore, the original 49 experimental designs were repeated three times at each wind speed level, resulting in a total of 147 experiments.

2.2. Boundary Condition Settings

(1) Governing Equations

(1) Energy Equation

In ANSYS 2024 Fluent software, for conducting a numerical simulation of convective heat transfer, it is essential to activate the energy equation. The general form of the energy equation commonly used in the software is as follows:

$$\frac{\partial}{\partial t}(\rho(e + \frac{v^2}{2})) + \nabla(\rho v(h + \frac{v^2}{2})) = \nabla \cdot (k_{eff} \nabla T - \sum_j h_j \bar{J}_j + \tau_{eff} \cdot \bar{v}) + S_h \tag{2}$$

$$k_{eff} = k + k_t \tag{3}$$

where ρ is the material density (kg/m³), v is velocity (m/s), k_{eff} is the effective thermal conductivity, k is the thermal conductivity of the material, and k_t is the turbulent thermal conductivity, defined according to the specific turbulence model employed. The units for thermal conductivity are all W/(m K). J_j is the diffusion flux of the j -th component. T is the temperature (K), and ∇ is the gradient of a variable, meaning the partial derivatives of the variable in the x , y , and z directions, respectively. The internal energy of the material e can be calculated as follows:

$$e = h - \frac{p_{op} + p}{\rho} \tag{4}$$

where p_{op} and p are the gauge pressure and operating pressure (Pa), respectively, and h denotes the enthalpy of the material (kJ/kg):

$$h = \sum_j Y_j h_j \tag{5}$$

$$h_j = \int_{T_{ref}}^T c_{p,j} dT \tag{6}$$

where Y_j and h_j are the mass fraction and enthalpy of the j -th substance, respectively. T_{ref} is the reference temperature (K), and $c_{p,j}$ is the specific heat capacity of the j -th substance (J/(kg K)). The three terms on the right side of the equation represent energy transfer due to thermal conduction, material diffusion, and viscous dissipation, respectively. S_h is the volumetric heat source.

In the solid region, the form of the energy transport equation used in the software is as follows:

$$\frac{\partial}{\partial t}(\rho h) + \nabla \cdot (\vec{v} \rho h) = \nabla \cdot (k \nabla T) + S_h \quad (7)$$

(2) Turbulence Model

This study employs the realizable k - ε turbulence model to conduct numerical simulation experiments on a fin-tube heat exchanger.

The realizable k - ε model constrains the Reynolds stress, ensuring that it aligns with the values observed in physical experiments—a limitation presented in the standard k - ε and RNG k - ε models. This advantage allows more accurate calculation of the spreading rate of the planar and round jets in numerical simulations. Additionally, in simulations of rotating flows, boundary layers with directional pressure, and separated flows, the realizable k - ε model provides results that more closely match real-world values.

The governing equations for the realizable k - ε turbulence model in the Fluent software are as follows:

The expression for the turbulent kinetic energy k is:

$$\frac{\partial}{\partial t}(\rho k) + \frac{\partial}{\partial x_j}(\rho k u_j) = \frac{\partial}{\partial x_j} \left[\left(\mu + \frac{\mu_t}{\sigma_k} \right) \frac{\partial k}{\partial x_j} \right] + G_k + G_b - \rho \varepsilon - Y_M + S_k \quad (8)$$

The equation for the turbulent dissipation rate ε is expressed as follows:

$$\frac{\partial}{\partial t}(\rho \varepsilon) + \frac{\partial}{\partial x_j}(\rho \varepsilon u_j) = \frac{\partial}{\partial x_j} \left[\left(\mu + \frac{\mu_t}{\sigma_\varepsilon} \right) \frac{\partial \varepsilon}{\partial x_j} \right] + \rho C_1 S \varepsilon - \rho C_2 \frac{\varepsilon^2}{k + \sqrt{\nu \varepsilon}} + C_{1\varepsilon} \frac{\varepsilon}{k} C_{3\varepsilon} G_b + S_\varepsilon n \quad (9)$$

where

$$C_1 = \max \left[0.43, \frac{\eta}{\eta + 5} \right], \eta = S \frac{k}{\eta + 5}, S = \sqrt{2 S_{ij} S_{ij}} \quad (10)$$

where μ_t is the turbulent viscosity, G_k is the generation of turbulent kinetic energy due to the mean velocity gradient, G_b is the generation of turbulent kinetic energy due to buoyancy, Y_M is the contribution of fluctuating dilation in compressible turbulence to the overall dissipation, C_2 and $C_{1\varepsilon}$ are constants, σ_k and σ_ε are the turbulent Prandtl numbers for k and ε , respectively, and S_k and S_ε are custom source terms.

(2) Boundary Condition

To efficiently arrange the computational domain, thereby conserving computational resources and enhancing computational accuracy, this paper investigates three different computational units. Figure 2 illustrates the computational unit and domain of an integral-type spiral finned tube, where Figure 2a displays the arrangement of the staggered finned tube bundle. Considering that the finned tube contains multiple repetitive units in the transverse direction and assuming that the cold air at the inlet is uniformly distributed transversely, three simplified computational domain methods are commonly adopted in most studies: Computational Unit 1 [20,21], Computational Unit 2 [22], and Computational Unit 3 [23]. These simplified computational units effectively reduce computational time and resource consumption without sacrificing the accuracy of the simulation results.

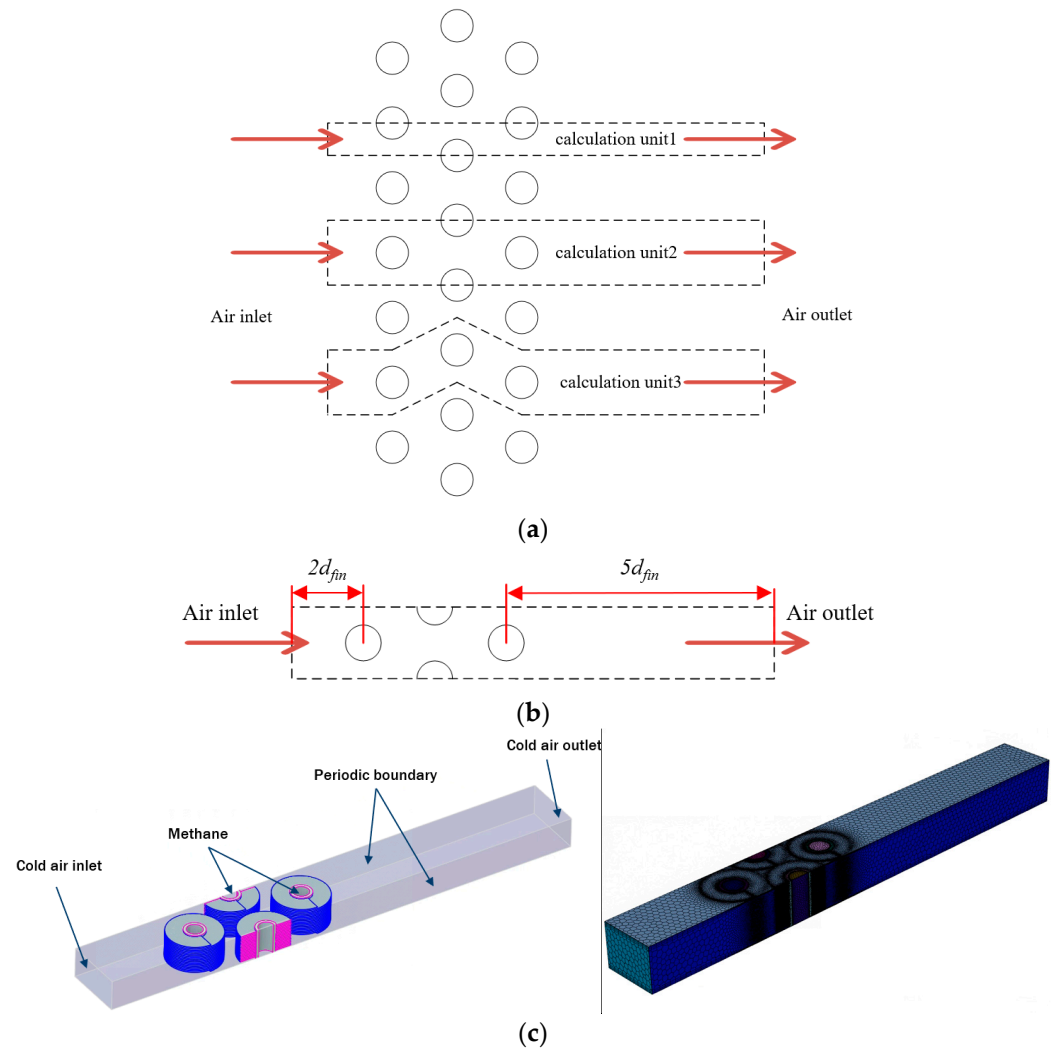


Figure 2. Structural parameters of fins and tube bundles for different simulation objects. (a) The arrangement of the staggered finned tube bundle; (b) Computational Unit 2 for simulation analysis; (c) the specific settings of the boundary conditions.

In the process of selecting computational units, Computational Unit 1 is deemed unsuitable for this study due to its boundary topology being orthogonal to the transverse direction, which does not meet the periodic conditions. Computational Unit 3 also does not fit the scope of this research since this study aims to explore minimal transverse and longitudinal spacing, which could lead to interference between the fluid and fin structures, potentially causing the fin to penetrate the fluid domain's periodic surface. Therefore, this research primarily relies on Computational Unit 2 for simulation analysis, as illustrated in Figure 2b.

To ensure that the air is evenly distributed upon entry, the length of the air inlet section is designed to be twice the outer diameter of the fins of a single spiral finned tube. Similarly, to reduce the impact of backflow at the outlet, the length of the air outlet section is set to be five times the outer diameter of the fins of a single spiral finned tube. The specific settings of the boundary conditions are illustrated in Figure 2c.

The simulation setup for the heat exchanger in this study is configured as follows: the internal flow gas inlet is set as a mass flow inlet, with a specified mass flow rate of 0.21 kg/s, an inlet temperature of 85 °C, and a pressure of 16 MPa. The outlet is set as a pressure outlet to simulate the pressure release conditions typical of operational environments.

For the external airflow, the inlet is specified as a velocity inlet with an inlet temperature of 35 °C to ensure a constant air velocity within the computational domain, while

the outlet is configured as a pressure outlet. The heat exchanger surface is defined as a fluid–solid coupling interface to accurately simulate heat transfer between the external air and the heat exchanger, as well as the thermal response of the exchanger itself. To emulate the continuous arrangement of the finned tubes commonly found in practical applications, periodic boundary conditions are applied to the lateral boundaries of the computational domain. This approach enables the performance assessment of a single unit, from which the behavior of the entire structure under similar operating conditions can be inferred. The details of the boundary conditions are provided in Table 4.

Table 4. Boundary condition settings.

| Region | Internal Domain | External Domain |
|------------------------|-----------------|-----------------|
| Substance | Methane | Air |
| Inlet Temperature (°C) | 85 | 35 |
| Inlet Type | Mass Flow Inlet | Velocity Inlet |
| Outlet Type | Pressure Outlet | Pressure Outlet |
| Mass Flow Rate (kg/s) | 0.21 | - |
| Gauge Pressure (MPa) | 16 | 0 |

The internal flow gas is defined as methane, while the external gas is set as air, and the heat exchanger material is specified as 304 stainless steel. The material parameters are detailed in Table 5. Given that the selected computational length of the internal fluid is relatively short, the pressure and temperature variations of the methane are minimal. Thus, the methane can be approximately treated as an incompressible gas, allowing the parameters of the methane under the operating conditions to be set accordingly [24].

Table 5. Material parameters table.

| Material Name | Methane | 304 Stainless Steel |
|-----------------------------------|--------------------------|---------------------|
| Density (kg/m ³) | 92.1218 | 7930 |
| Specific heat capacity (J/(kg K)) | 3084.7 | 500 |
| Thermal conductivity (W/(m K)) | 0.0626 | 16.2 |
| Viscosity (kg/(m s)) | 1.72943×10^{-5} | - |

2.3. Mesh Independence Verification

During the meshing process of the heat exchanger model using Fluent meshing, the poly-hexcore meshing method was employed. This type of mesh is particularly suitable for simulating thin-walled heat exchanger fins due to its advantages in handling near-gradient complexities and reducing numerical diffusion effects. As gradients are more pronounced near the forced heat transfer walls than in areas further from the walls, a denser mesh configuration is required near the fluid–solid coupling surfaces to enhance the accuracy of the simulation results. Consequently, boundary layers were specifically set up in these areas.

To ensure both the accuracy of the computational results and the optimization of the computation time, this study conducted mesh independence verification of the model grid. The specific verification data and comparison results are shown in Table 6.

Table 6. Mesh independence verification table.

| Number of meshes | 253.8×10^4 | 305.6×10^4 | 572.7×10^4 |
|------------------|---------------------|---------------------|---------------------|
| <i>Nu</i> | 9.210 | 9.193 | 9.165 |
| ΔP | 20.368 | 20.384 | 20.396 |

In this paper, mesh independence verification for the heat exchanger was conducted using three different sets of mesh counts. The verification involved comparing the Nusselt

number (Nu) values and the pressure differences (ΔP) between the air inlet and outlet at various mesh counts. When the number of meshes increased from 253.8×10^4 to 305.6×10^4 , the decrease in the Nu was only 0.017, corresponding to a relative error of about 0.2%; at the same time, the increase in the pressure difference (ΔP) was merely 0.016 Pa, with a relative error of about 0.08%. When the number of meshes was further increased to 572.7×10^4 , the Nu value decreased by 0.028, with a relative error of 0.3%; ΔP increased by 0.12 Pa, with a relative error of 0.59%.

The results indicate that with an increase in the number of meshes, the changes in both the Nu and the pressure difference ΔP are minimal, with all errors below 1%. Therefore, to ensure computational accuracy and cost-effectiveness, selecting a mesh count ranging from 250×10^4 to 30×10^4 is appropriate. This range is sufficient to guarantee the accuracy of the simulation results while avoiding the unnecessary consumption of computational resources.

3. Analysis and Evaluation of Finite Element Simulation Results

3.1. Evaluation Metrics for Spiral Finned Tube Heat Transfer Performance

Kays and London's j - f factor method is a commonly used approach for evaluating heat exchanger performance [25]. In this method, j represents the heat transfer factor, which characterizes the heat transfer capability of the heat exchanger, while f denotes the friction factor, which quantifies the resistance to external air flow around the heat exchanger.

The expression for the heat transfer factor j is as follows:

$$j = \frac{Nu}{Re \cdot Pr^{1/3}} \quad (11)$$

$$Re = \frac{\rho v_{max} De}{\mu_0} \quad (12)$$

$$Pr = \frac{\mu_0 C_p}{\lambda_0} \quad (13)$$

where Re is the Reynolds number, v_{max} is the velocity at the minimum cross-section of the fin (m/s), μ_0 is the dynamic viscosity of air (kg/m·s), Pr is the Prandtl number, which is typically 0.7 for air, C_p is the specific heat capacity at constant pressure, and Nu represents the Nusselt number:

$$Nu = \frac{h_0 De}{\lambda_0} \quad (14)$$

where h_0 is the average convective heat transfer coefficient with units of W/(m²·K), λ_0 is the thermal conductivity of the fluid with units of W/(m·K), and De represents the characteristic length (m).

For complex shapes, the characteristic length can be defined as the volume of the fluid divided by the surface area, i.e.:

$$De = \frac{V_f}{A_f} \quad (15)$$

where V_f represents the volume of the fluid (m³), and A_f represents the surface area of the fluid (m²).

The formula for calculating the average convective heat transfer coefficient h_0 is as follows:

$$h_0 = \frac{Q}{A_0(\bar{T}_{wall} - T_\infty)} \quad (16)$$

$$Q = \rho c_p A_{in} v_{in} \Delta T \quad (17)$$

where Q is the heat flow rate (W), ρ is the density (kg/m³), A_{in} is the inlet cross-sectional area (m²), v_{in} is the inlet velocity (m/s), ΔT is the temperature difference between the inlet and outlet (K), A_0 is the total heat transfer area (m²), and \bar{T}_{wall} and T_∞ are the

average wall temperature (K) and average air temperature (K), which can be calculated by Equations (18) and (19), respectively:

$$\bar{T}_{wall} = \frac{1}{A_0} \int_{A_0} T_{wall} dA \quad (18)$$

$$T_{\infty} = \frac{1}{2}(T_{in} - T_{out}) \quad (19)$$

The greater the pressure difference between the inlet and outlet of the fluid domain, the greater the resistance of the heat exchanger to the fluid. Kays et al. [25] proposed the resistance factor f , which is used to evaluate the resistance performance of the heat exchanger. The expression for f is as follows:

$$f = \frac{2\Delta P \cdot De}{\rho v_{max}^2 L} \quad (20)$$

where ΔP is the pressure drop between the inlet and outlet, and L is the length in the flow direction.

In the heat exchanger design and performance evaluation, heat transfer efficiency and pressure loss are two key factors that influence each other. High-efficiency heat transfer often comes with significant pressure loss, and vice versa. Therefore, optimizing heat transfer efficiency alone or simply reducing resistance cannot comprehensively improve the performance of the heat exchanger. In practical applications, a multi-objective optimization strategy can be employed to find the optimal balance between the two factors.

To fully assess the performance of a heat exchanger, a comprehensive evaluation indicator JF is introduced [26], which takes into account both heat transfer efficiency and pressure loss. The comprehensive performance evaluation indicator is as follows:

$$JF = \frac{j/j_0}{(f/f_0)^{1/3}} \quad (21)$$

where j_0 and f_0 are the heat transfer factor j and the resistance factor f of the heat exchanger before optimization.

3.2. Analysis of Heat Transfer Performance Under Different Wind Speeds

In this subsection, the first five sets of schemes from the orthogonal table are used as examples. The flow state, heat transfer performance, and pressure loss of the helical finned tube bundle are analyzed separately.

(1) Analysis of heat transfer performance

The Nusselt number (Nu) is a dimensionless parameter used to assess convective heat transfer efficiency. An increase in the Nu indicates improved convective heat transfer. The heat transfer factor j evaluates the heat transfer performance by incorporating the effects of the fluid flow, heat transfer mode, and heat transfer area. Figure 3 illustrates the variations in the Nu and the heat transfer factor j for the first five sets of schemes listed in the orthogonal table in Table 2 under different wind speeds.

The Nu gradually rises as the wind speed increases, indicating that the convective heat transfer improves with increasing wind speed. However, the heat transfer factor j decreases as wind speed increases, which is consistent with its calculation formula. Additionally, the rate of increase in the Nu slows down with increasing wind speed, showing that the improvement in heat transfer efficiency is limited at high wind speeds. For multiple groups of heat exchangers, high wind speeds widen the differences in Nu , indicating that the performance disparities among the different heat exchangers become more pronounced under extreme conditions. The decrease in j is mainly due to the enhanced convective flow caused by increased wind speed, which intensifies heat exchange between the heat transfer surface and the fluid but also increases thermal resistance. This is primarily because higher

wind speeds reduce the residence time of the fluid over the heat transfer surface and decrease the effective heat transfer area and may lead to turbulent conditions.

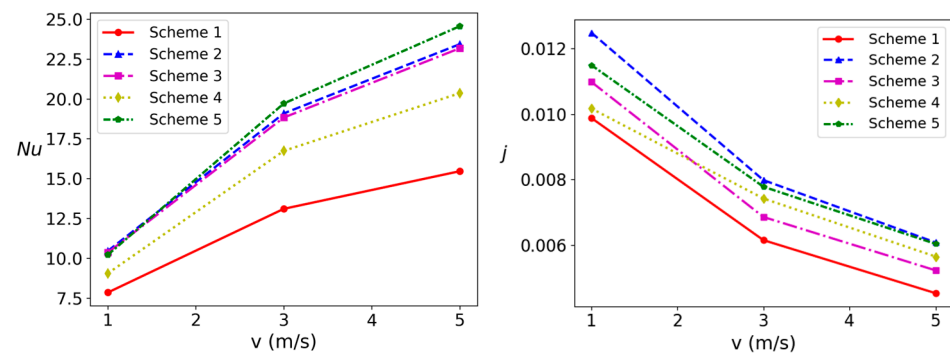


Figure 3. Comparison of heat transfer performance for different groups of heat exchangers.

(2) Analysis of pressure loss

In heat exchanger design, pressure loss caused by external air flow is a critical consideration. This loss typically manifests as a pressure drop, which is the decrease in pressure due to friction and flow resistance as the fluid passes through pipes or equipment. Figure 4 reflects the changes in the air pressure drop on the surface of the heat exchangers for the first five sets of schemes under different wind speeds.

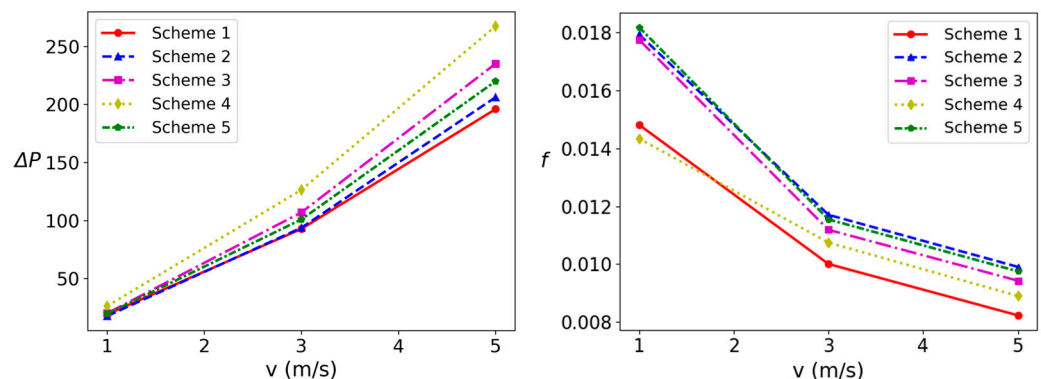


Figure 4. Comparison of resistance performance for different groups of heat exchangers.

The air pressure drop in Figure 4 increases with rising wind speed, indicating that the increase in air kinetic energy at higher wind speeds leads to enhanced flow resistance. Additionally, as wind speed increases, the differences in the pressure drop between different groups of heat exchangers expand, as the variations in resistance performance become more pronounced at higher wind speeds. Furthermore, the resistance factor f gradually decreases as the wind speed increases. This is because the resistance factor f is primarily influenced by the increase in flow velocity, and the effect of increased wind speed on reducing the f value outweighs the impact of the increased pressure drop.

3.3. Range Analysis

The range analysis of orthogonal experiments is a statistical method to quickly identify the differences in the responses of various factors at different levels. This helps in the determination of the influence degree of each factor on the experimental results and their optimal combinations.

In this study, range analysis is used to evaluate several key structural parameters affecting the performance of finned tube heat exchangers, including fin pitch, fin thickness, fin height, base tube diameter, transverse spacing, and longitudinal spacing. This analysis involves calculating the mean performance responses of these parameters at different levels.

By analyzing the range of response means, the parameters that most significantly affect the heat exchanger performance can be effectively identified, and the optimal setting levels of each parameter can be determined. The value K represents the sum of the experimental data for each factor at each level and can be expressed as:

$$K = \sum_{i=1}^n K_i \tag{22}$$

where n is the number of repetitions at each level.

To assess the influence of each parameter on the results, the range R is calculated as the difference between the maximum and minimum values of the average performance measure K_{avg} for each parameter. The range R_j for the j -th factor can be expressed as:

$$R_j = \max(K_{avg_{ij}}) - \min(K_{avg_{ij}}) \tag{23}$$

where $K_{avg_{ij}}$ is the mean of the values corresponding to the i -th level of the j -th factor.

(1) Range analysis of air inlet and outlet pressure difference

The range analysis of the air inlet and outlet pressure difference for each influencing factor is shown in Table 7. The optimal level of each factor corresponds to a maximum K_{avg} value.

Table 7. Range analysis results for pressure difference.

| Factors | Levels | ΔP | | | | | | |
|------------|--------|------------|----------------|----------|----------------|-----------------|------------|------------|
| | | S (mm) | t_{fin} (mm) | h (mm) | d_{out} (mm) | t_{tube} (mm) | S_h (mm) | S_z (mm) |
| K Value | 1 | 1722.728 | 1177.33 | 1503.01 | 1361.259 | 1393.556 | 1641.154 | 1432.602 |
| | 2 | 1474.839 | 1342.971 | 1422.156 | 1402.075 | 1439.37 | 1479.304 | 1467.248 |
| | 3 | 672.018 | 749.35 | 701.068 | 736.066 | 710.436 | 696.394 | 717.028 |
| | 4 | 596.304 | 831.894 | 701.971 | 727.976 | 750.367 | 624.234 | 702.62 |
| | 5 | 545.594 | 909.94 | 683.279 | 784.108 | 717.755 | 570.397 | 691.986 |
| Kavg Value | 1 | 123.052 | 84.095 | 107.358 | 97.233 | 99.54 | 117.225 | 102.329 |
| | 2 | 105.346 | 95.926 | 101.583 | 100.148 | 102.812 | 105.665 | 104.803 |
| | 3 | 96.003 | 107.05 | 100.153 | 105.152 | 101.491 | 99.485 | 102.433 |
| | 4 | 85.186 | 118.842 | 100.282 | 103.997 | 107.195 | 89.176 | 100.374 |
| | 5 | 77.942 | 129.991 | 97.611 | 112.015 | 102.536 | 81.485 | 98.855 |
| Best Level | | 1 | 5 | 1 | 5 | 4 | 1 | 2 |
| R | | 45.11 | 45.896 | 9.747 | 14.783 | 7.656 | 35.74 | 5.948 |

From the range analysis results, the influence degree of the factors on ΔP from large to small is t_{fin} ($R: 45.896$) > S ($R: 45.11$) > S_h ($R: 35.74$) > d_{out} ($R: 14.783$) > h ($R: 9.747$) > t_{tube} ($R: 7.656$) > S_z ($R: 5.948$). By comparing the K_{avg} values of each parameter, it can be found that S has the maximum K_{avg} value at level 1, while t_{fin} , h , d_{out} , t_{tube} , S_h , and S_z have the maximum K_{avg} values at levels 5, 1, 5, 4, 1, and 2, respectively. Therefore, the optimal combination is $S_1, t_{fin5}, h_1, d_{out5}, t_{tube4}, S_{h1}, S_{z2}$.

(2) Range analysis of Nusselt number

The range analysis of the Nusselt number Nu for each influencing factor is shown in Table 8.

From the range analysis results, the influence degree of the factors on the Nu from large to small is h ($R: 5.161$) > t_{fin} ($R: 3.67$) > S_h ($R: 2.973$) > S_z ($R: 0.675$) > d_{out} ($R: 0.512$) > t_{tube} ($R: 0.404$) > S ($R: 0.356$). By comparing the K_{avg} values of each parameter, it can be found that S has the maximum K_{avg} value at level 5, while t_{fin} , h , d_{out} , t_{tube} , S_h and S_z have the maximum K_{avg} values at levels 5, 1, 4, 2, 1, and 1, respectively. Therefore, the optimal combination is $S_5, t_{fin5}, h_1, d_{out4}, t_{tube2}, S_{h1}, S_{z1}$.

Table 8. Range analysis results for Nusselt number.

| Factors | Levels | Nu | | | | | | |
|------------|--------|---------|----------------|---------|----------------|-----------------|------------|------------|
| | | S (mm) | t_{fin} (mm) | h (mm) | d_{out} (mm) | t_{tube} (mm) | S_h (mm) | S_z (mm) |
| K Value | 1 | 256.663 | 232.474 | 284.509 | 256.071 | 256.573 | 271.277 | 259.915 |
| | 2 | 252.404 | 248.648 | 265.876 | 256.385 | 257.046 | 262.599 | 253.47 |
| | 3 | 127.454 | 132.697 | 122.807 | 127.682 | 125.697 | 124.492 | 129.14 |
| | 4 | 127.929 | 137.4 | 113.828 | 128.294 | 126.874 | 119.951 | 125.234 |
| | 5 | 128.695 | 141.926 | 106.124 | 124.712 | 126.955 | 114.826 | 125.386 |
| Kavg Value | 1 | 18.333 | 16.605 | 20.322 | 18.291 | 18.327 | 19.377 | 18.565 |
| | 2 | 18.029 | 17.761 | 18.991 | 18.313 | 18.36 | 18.757 | 18.105 |
| | 3 | 18.208 | 18.957 | 17.544 | 18.24 | 17.957 | 17.785 | 18.449 |
| | 4 | 18.276 | 19.629 | 16.261 | 18.328 | 18.125 | 17.136 | 17.891 |
| | 5 | 18.385 | 20.275 | 15.161 | 17.816 | 18.136 | 16.404 | 17.912 |
| Best Level | | 5 | 5 | 1 | 4 | 2 | 1 | 1 |
| R | | 0.356 | 3.67 | 5.161 | 0.512 | 0.404 | 2.973 | 0.675 |

(3) Range analysis of heat transfer factor

The range analysis of the heat transfer factor j for each influencing factor is shown in Table 9.

Table 9. Range analysis results for heat transfer factor.

| Factors | Levels | j | | | | | | |
|------------|--------|---------|----------------|---------|----------------|-----------------|------------|------------|
| | | S (mm) | t_{fin} (mm) | h (mm) | d_{out} (mm) | t_{tube} (mm) | S_h (mm) | S_z (mm) |
| K Value | 1 | 0.1091 | 0.10251 | 0.10937 | 0.10909 | 0.10692 | 0.11176 | 0.10731 |
| | 2 | 0.10593 | 0.10448 | 0.10851 | 0.10593 | 0.10537 | 0.10885 | 0.10373 |
| | 3 | 0.05136 | 0.05375 | 0.05172 | 0.05157 | 0.05187 | 0.0507 | 0.05294 |
| | 4 | 0.05094 | 0.05324 | 0.0497 | 0.05218 | 0.05171 | 0.04878 | 0.05139 |
| | 5 | 0.04969 | 0.05304 | 0.04772 | 0.04825 | 0.05114 | 0.04693 | 0.05165 |
| Kavg Value | 1 | 0.00779 | 0.00732 | 0.00781 | 0.00779 | 0.00764 | 0.00798 | 0.00767 |
| | 2 | 0.00757 | 0.00746 | 0.00775 | 0.00757 | 0.00753 | 0.00778 | 0.00741 |
| | 3 | 0.00734 | 0.00768 | 0.00739 | 0.00737 | 0.00741 | 0.00724 | 0.00756 |
| | 4 | 0.00728 | 0.00761 | 0.0071 | 0.00745 | 0.00739 | 0.00697 | 0.00734 |
| | 5 | 0.0071 | 0.00758 | 0.00682 | 0.00689 | 0.00731 | 0.0067 | 0.00738 |
| Best Level | | 1 | 3 | 1 | 1 | 1 | 1 | 1 |
| R | | 0.00069 | 0.00036 | 0.00099 | 0.0009 | 0.00033 | 0.00128 | 0.00032 |

From the range analysis results, the influence degree of the factors on j from large to small is S_h ($R: 0.00128$) > h ($R: 0.00099$) > d_{out} ($R: 0.0009$) > S ($R: 0.00069$) > t_{fin} ($R: 0.00036$) > t_{tube} ($R: 0.00033$) > S_z ($R: 0.00032$). By comparing the $Kavg$ values of each parameter, it can be found that S has the maximum $Kavg$ value at level 1, while t_{fin} , h , d_{out} , t_{tube} , S_h and S_z have the maximum $Kavg$ values at levels 3, 1, 1, 1, 1, and 1, respectively. Therefore, the optimal combination is $S_1, t_{fin3}, h_1, d_{out1}, t_{tube1}, S_{h1}, S_{z1}$.

(4) Range analysis of resistance factor

The range analysis of the resistance factor f for each influencing factor is shown in Table 10.

From the range analysis results, the influence degree of the factors on f from large to small is h ($R: -0.00116$) > t_{tube} ($R: -0.0004$) > d_{out} ($R: -0.00034$) > S ($R: -0.00029$) > S_z ($R: -0.00028$) > S_h ($R: -0.00022$) > t_{fin} ($R: -0.00011$). By comparing the $Kavg$ values of each parameter, it can be found that S has the maximum $Kavg$ value at level 4, while t_{fin} , h , d_{out} , t_{tube} , S_h , and S_z have the maximum $Kavg$ values at levels 5, 1, 1, 1, 2, and 5, respectively. Therefore, the optimal combination is $S_4, t_{fin5}, h_1, d_{out1}, t_{tube1}, S_{h2}, S_{z5}$.

Table 10. Range analysis results for resistance factor.

| Factors | Levels | <i>f</i> | | | | | | |
|------------|--------|---------------|-----------------------------|---------------|-----------------------------|------------------------------|---------------------------|---------------------------|
| | | <i>S</i> (mm) | <i>t_{fin}</i> (mm) | <i>h</i> (mm) | <i>d_{out}</i> (mm) | <i>t_{tube}</i> (mm) | <i>S_h</i> (mm) | <i>S_z</i> (mm) |
| K Value | 1 | 0.14922 | 0.15027 | 0.15809 | 0.15278 | 0.15226 | 0.14986 | 0.14954 |
| | 2 | 0.15156 | 0.15075 | 0.15346 | 0.14944 | 0.1512 | 0.15275 | 0.14962 |
| | 3 | 0.07511 | 0.07546 | 0.07284 | 0.07525 | 0.07586 | 0.07483 | 0.0757 |
| | 4 | 0.07662 | 0.07541 | 0.0725 | 0.07628 | 0.07515 | 0.07508 | 0.07621 |
| | 5 | 0.07527 | 0.07589 | 0.0709 | 0.07404 | 0.07332 | 0.07526 | 0.07672 |
| Kavg Value | 1 | 0.01066 | 0.01073 | 0.01129 | 0.01091 | 0.01088 | 0.0107 | 0.01068 |
| | 2 | 0.01083 | 0.01077 | 0.01096 | 0.01067 | 0.0108 | 0.01091 | 0.01069 |
| | 3 | 0.01073 | 0.01078 | 0.01041 | 0.01075 | 0.01084 | 0.01069 | 0.01081 |
| | 4 | 0.01095 | 0.01077 | 0.01036 | 0.0109 | 0.01074 | 0.01073 | 0.01089 |
| | 5 | 0.01075 | 0.01084 | 0.01013 | 0.01058 | 0.01047 | 0.01075 | 0.01096 |
| Best Level | | 4 | 5 | 1 | 1 | 1 | 2 | 5 |
| R | | 0.00029 | 0.00011 | 0.00116 | 0.00034 | 0.0004 | 0.00022 | 0.00028 |

4. Prediction Model of Heat Transfer Performance Based on Spiral Finned Tube Parameters

In this study, 49 different geometrical configurations of spiral finned tubes were constructed, and 147 experiments were carried out using the orthogonal design method under three different wind speed conditions. These experiments provide insights into the heat transfer efficiency and pressure distribution characteristics of the heat exchanger on the air side, aiming to reveal the critical relationship between the structural features of the heat exchanger and its heat exchange performance and flow resistance. The parameters that comprehensively reflect the performance of the heat exchanger are considered, such as the Nusselt number (*Nu*), pressure difference between the inlet and outlet (ΔP), and maximum wind velocity (*V_{max}*) flowing through the smallest cross-section. In order to optimize the heat transfer and resistance performance of the finned tubes, regression models are introduced in this subsection to predict the heat transfer factor and resistance factor.

4.1. Theoretical Basis of Regression Modeling

The main goal of regression modeling is to establish a quantitative relationship between the dependent variable and one or more independent variables. In the field of engineering and scientific research, the exploration of this relationship is crucial as it not only promotes the understanding of variable interactions but also helps to predict future trends. For datasets with small sample sizes, the selection of an appropriate regression model is especially critical. The following regression models are often used to tackle the problem of small-sample datasets.

(1) Random forest regression

Random forest regression is an integrated model consisting of multiple decision trees. Each decision tree is modeled by randomly selecting samples and features from the original dataset during training, and the final output is the average of the outputs of all the decision trees. Its prediction model can be expressed as:

$$\hat{y} = \frac{1}{B} \sum_{b=1}^B T_b(x) \tag{24}$$

where \hat{y} is the predicted value, *B* is the number of decision trees, and *T_b* is the prediction of the input by the *x*-th decision tree.

(2) Support vector regression

SVR maps a low-dimensional space to a high-dimensional space through a nonlinear function transformation and finds a linearly separable hyperplane in the high-dimensional

space, aiming to minimize the distance between the fitting point and the farthest sample point in the hyperplane. An SVR function can be expressed as:

$$f(x) = \langle w, x \rangle + b \quad (25)$$

where $\langle w, x \rangle$ denotes the dot product of the weight vector w and the feature vector x , and b is the bias term. For the nonlinear problem, by introducing the kernel function $K(x, x_i)$, the SVR model can be expressed as:

$$f(x) = \sum_{i=1}^n (\alpha_i - \alpha_i^*) K(x, x_i) + b \quad (26)$$

where α_i and α_i^* are the Lagrange multipliers, and n is the number of support vectors.

(3) Kriging regression

The kriging model is a regression method based on optimal linear unbiased prediction and is mainly used for spatial interpolation of geostatistical data. Its prediction formula is:

$$\hat{Z}(x_0) = \mu + \sum_{i=1}^n \lambda_i (Z(x_i) - \mu) \quad (27)$$

where $\hat{Z}(x_0)$ is the predicted value of the location, μ is the global average, λ_i is the weight, $Z(x_i)$ is the observed value of the known location, and n is the number of known data points. The weight λ_i is calculated from the spatial covariance or semi-variance function.

4.2. Regression Modeling and Evaluation

The fin pitch, fin thickness, fin height, base tube diameter, base tube thickness, transverse spacing, longitudinal distance, and wind speed are used as input variables to construct the prediction models for the heat transfer factor j and the resistance factor f , respectively, based on the commonly used random forest, support vector machine, and kriging models.

The feasibility of each prediction model is assessed using the root mean square error (RMSE), mean absolute percentage of error (MAPE) and coefficient of determination (R^2), as described in Equations (27)–(29), respectively. A total of $149 \times 0.8 = 119$ sets of data are defined as the training set, and the remaining 30 sets of data are defined as the testing set. Table 11 lists the main parameters of the random forest, support vector machine, and kriging models.

$$\text{RMSE} = \sqrt{\frac{1}{n} \sum_{i=1}^n (y_i - \hat{y}_i)^2} \quad (28)$$

$$R^2 = 1 - \frac{\sum_i (\hat{y}_i - y_i)^2}{\sum_i (\bar{y}_i - y_i)^2} \quad (29)$$

$$\text{MAPE} = \frac{100\%}{n} \sum_{i=1}^n \left| \frac{\hat{y}_i - y_i}{y_i} \right| \quad (30)$$

where n is the sample size, y_i is the true value, and \hat{y}_i is the predicted value.

The j factors and f factors of the testing dataset were predicted using random forest, and the true and predicted values of the j factor and f factor are compared in Figures 5a and 5b, respectively.

Support vector machines were used to predict the j factors and f factors of the testing dataset, and the true and predicted values of the j factor and f factor are compared in Figures 6a and 6b, respectively. The prediction accuracy of the SVR model exceeds that of the random forest model.

Table 11. Setting of the main parameters of each algorithm.

| Model | Parameter | Parameter Value |
|---------------|---|---|
| Random forest | Number of decision trees | 300 |
| | Minimum number of leaves | 1 |
| | Randomly selected feature variables | 8 |
| SVR | Kernel function | Radial basis function (RBF) |
| | Penalty factor | 4 |
| | RBF parameter | 0.8 |
| Kriging | Correlation coefficient vector θ | $(lob + upb)/2$ |
| | Lower boundary of θ lob | [2.2, 0.3, 13.5, 25, 3, 0.5, 0.0001, 1] |
| | Upper boundary of θ upb | [3, 0.7, 21.5, 29, 5, 8.5, 8, 5] |
| | Correlation function | Linear function |

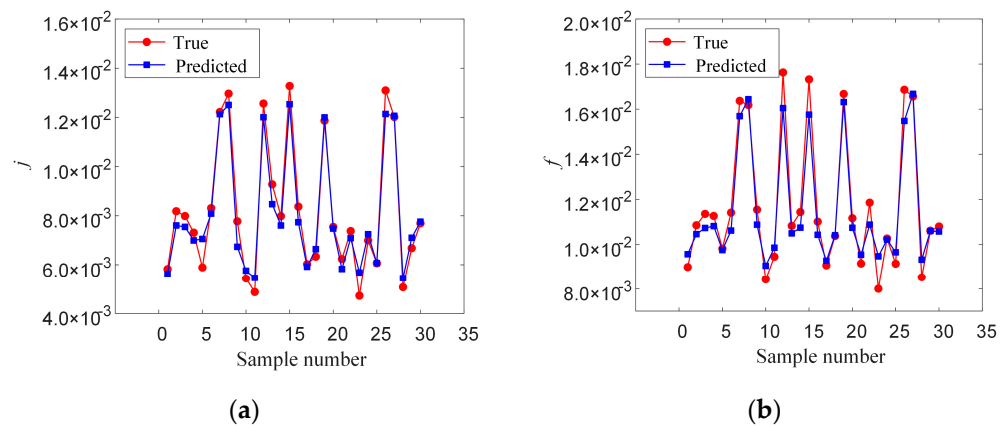


Figure 5. The j and f factors predicted by random forest modeling. (a) Comparisons of the predicted and actual j factors; (b) comparisons of the predicted and actual f factors.

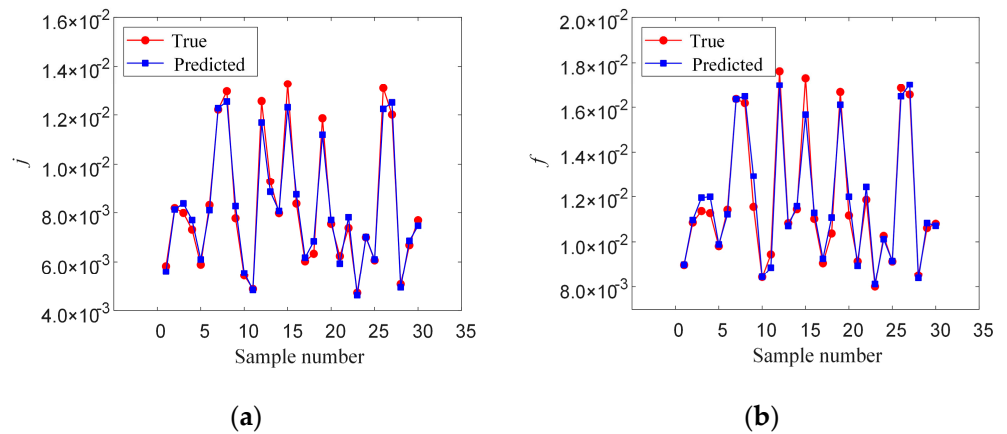


Figure 6. The j and f factors predicted by the SVR modeling. (a) Comparisons of the predicted and actual j factors; (b) comparisons of the predicted and actual f factors.

The kriging model was used to predict the j -factor and f -factor of the testing dataset, and the true and predicted values of the j -factor and f -factor are compared in Figures 7a and 7b, respectively. The prediction accuracy of the SVR model still exceeds that of the kriging model.

Furthermore, the predictive performance of the regression models was evaluated on the testing data by combining Equations (27)–(29). Table 12 lists the RMSE, MAPE, and R^2 of the j factor and f factor computed based on each regression model. The SVR model corresponds to lower RMSE and MAPE values than those of the random forest and kriging models, and the R^2 values are higher than those of the random forest and kriging models,

indicating that the SVR model can better approximate the functional relationship between the input variables and the predictors. Therefore, the SVR model was finally selected as the regression prediction model for the heat transfer and resistance factors.

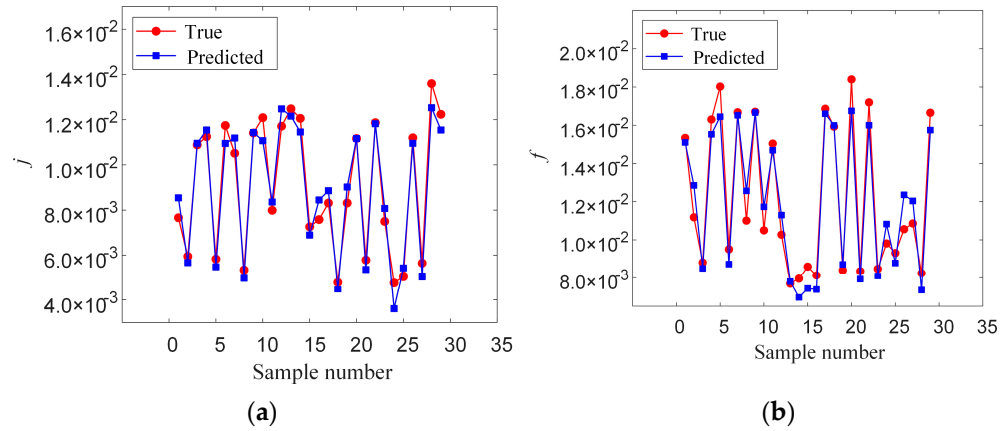


Figure 7. The j and f factors predicted by the kriging modeling. (a) Comparisons of the predicted and actual j factors; (b) comparisons of the predicted and actual f factors.

Table 12. Comparison of the calculation results of each regression model.

| Assessment Factor | Model | MAPE | RMSE | R ² |
|--------------------------|---------------|---------|--------|----------------|
| Heat transfer factor j | Random forest | 5.8645% | 0.0005 | 0.9597 |
| | SVR | 3.6080% | 0.0004 | 0.9764 |
| | Kriging model | 7.1954% | 0.0010 | 0.9331 |
| Resistance factor f | Random forest | 4.9623% | 0.0007 | 0.9406 |
| | SVR | 3.0665% | 0.0005 | 0.9665 |
| | Kriging model | 7.1954% | 0.0010 | 0.9331 |

5. Multi-Objective Optimization Modeling and Solution of Spiral Finned Tube Parameters

The optimization objective of this study is to enhance the overall performance of the spiral finned tube heat exchanger so that the heat transfer factor is as large as possible and the resistance factor is as small as possible. In Section 4, the regression prediction model of the heat transfer factor and resistance factor is established by taking the structural parameters of spiral finned tubes and wind speed as design variables. The use of the regression model for predicting the heat transfer factor and resistance factor can reduce the calculation cost of the optimization algorithm and improve the optimization efficiency. At the same time, considering that this study is to solve an optimization problem containing two optimization variables, j and f , the multi-objective problem is transformed into a single-objective optimization problem by using the comprehensive evaluation indicator described in Equation (21). Therefore, this study takes the comprehensive evaluation indicator JF as the optimization objective, and the genetic algorithm (GA) and SVR regression models are combined to solve the optimization model.

5.1. Introduction to Genetic Algorithms

The genetic algorithm (GA), a method inspired by biological evolution and natural selection, is widely used in optimization design fields. Optimization programs developed with GA offer notable advantages in optimizing the various heat exchangers used in eco-friendly vehicles. This approach has high practical value due to its potential for extension to the optimization of other components, including heat exchangers, especially those with lower degrees of nonlinearity. In optimization research, the GA’s ability to emulate evolutionary processes makes it a highly efficient and comparable method that is particularly well suited for the design optimization of various heat exchanger types [27].

The specific flowchart of the genetic algorithm is shown in Figure 8. The following are the key steps used in implementing a genetic algorithm to ensure its effectiveness.

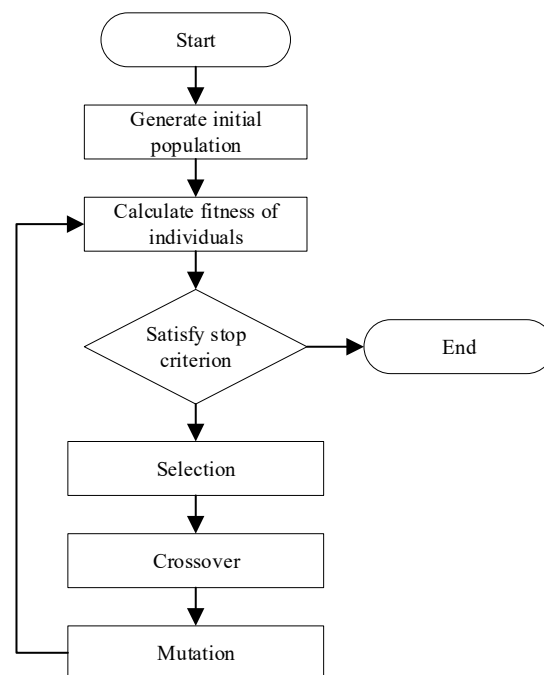


Figure 8. The flowchart of a genetic algorithm.

Initialization: When the algorithm starts, it first creates an initial population of potential solutions, each of which is represented by a coding sequence that is usually presented as the binary-encoded chromosome.

Evaluation: The performance of each individual in the population is evaluated through a fitness function that assigns a fitness score to an individual based on its performance, and a higher score indicates that the individual is more effective at solving the target problem.

Selection: A selection operation is implemented based on the fitness of an individual, and the roulette, tournaments, and other methods are commonly used to select superior individuals and pass on the better performing solutions to the next generation.

Crossover: Selected individuals produce offspring through a chromosome crossover operation, and chromosomes from two different individuals exchange segments with a predetermined probability during crossover, resulting in a new individual containing a mixture of characteristics.

Mutation: In order to increase the diversity of the population and avoid local optimization, certain genetic loci are randomly modified in the newly generated offspring, allowing the introduction of new features to explore a wider solution space.

Iteration: The above process is repeated with a new generation of individuals that gradually replaces the old population, and the whole algorithm continues to iterate until stopping conditions are met, such as meeting the maximum iteration number.

5.2. Multi-Objective Optimization Process

In this study, the heat transfer j -factor and the resistance f -factor were adopted as the key indicators for evaluating the heat dissipation performance and resistance of the spiral finned tube heat exchanger, resulting in two optimization objectives: the maximization of the heat transfer efficiency and the minimization of the fluid resistance. To achieve this goal, this study defined eight optimized design variables for spiral finned tubes, including fin pitch S , fin thickness t_{fin} , fin height h , base tube diameter d_{out} , base tube thickness t_{tube} , horizontal distance S_h , vertical distance S_z , and air velocity v . The range of values of the design variables is shown in Tables 1 and 2.

Given that the genetic algorithm is a single-objective optimization algorithm, it is necessary to convert the multi-objective optimization problem into a single-objective optimization problem. In this study, the comprehensive performance indicator JF of the spiral finned tube heat exchanger is selected as the optimization objective, and the specific definition of JF is shown in Equation (21). Accordingly, a single-objective optimization mathematical model is established, as shown in Equation (31):

$$\left\{ \begin{array}{l} \max F(X) = JF = \frac{j/j_0}{(f/f_0)^{\frac{1}{3}}} \\ \text{st. } 2.2 < S < 3 \\ 0.3 < t_{fin} < 0.7 \\ 13.5 < h < 21.5 \\ 25 < d_{out} < 29 \\ 3 < t_{tube} < 5 \\ 0.5 < S_h < 8.5 \\ 0 < S_z < 8 \end{array} \right. \quad (31)$$

where X is an eight-dimensional variable consisting of the structural control parameters of the spiral finned tube bundle and the wind speed.

In this study, a genetic algorithm model was constructed based on the above process. First, a fitness assessment was performed by directly defining the objective function as a fitness function. The initial population was randomly determined within the variation ranges, and the population members were subsequently decoded in order to compute the fitness of the individuals. The selection operation was performed using a roulette-based strategy, while the crossover and mutation operations were performed with the defined probabilities. The relevant parameters are listed in Table 12.

5.3. Multi-Objective Optimization Results

The optimization results of the genetic algorithm constructed in this study are described in Figure 9 and Table 13 describes the basic parameters of the genetic algorithm. Figure 9 shows the fitness curve during the iteration process, and Table 14 shows the specific fitness values at different iteration numbers.

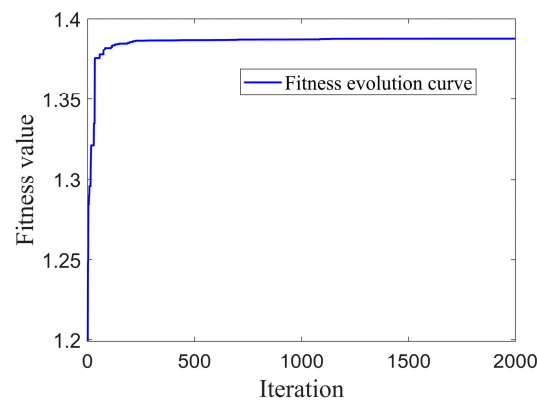


Figure 9. Adaptation curves during iteration.

Table 13. Setting of each parameter of the genetic algorithm.

| Parameter | Population Size | Chromosome Length | Crossover Rate | Variation Rate | Iteration Number |
|-----------|-----------------|-------------------|----------------|----------------|------------------|
| value | 300 | 400 | 0.3 | 0.01 | 1000 |

Table 14. Specific adaptation values at different numbers of iterations.

| Number of Iterations | 100 | 300 | 600 | 1000 | 1600 | 2000 |
|----------------------|--------|--------|--------|--------|--------|--------|
| Fitness Value | 1.3763 | 1.3858 | 1.3870 | 1.3878 | 1.3879 | 1.3879 |

The optimized structural parameters of the spiral finned tube are shown in Table 15, where pre-optimization means the initial model structural parameters and wind speed of the spiral finned tube, and post-optimization means the structural parameters obtained by using the genetic algorithm. Based on Table 15, the optimization results indicate that while the fin pitch S remains unchanged, the base tube diameter and thickness decrease slightly, whereas the fin height, transverse spacing, and longitudinal spacing decrease significantly. According to the range analysis of the heat transfer factor j and the range analysis of the resistance factor f in Section 3.3, and the conclusions drawn from Equation (21), these adjustments achieve a balanced configuration. Notably, when the fin height is at level $h1$, both the j and f values reach their highest points. Equation (21) applies a cubic root to f , thereby reducing its impact, which allows the JF factor to reach its maximum when the fin height is $h1$. For the transverse and longitudinal spacings, the optimal configuration approximates levels S_h1 and S_z1 , with the j factor being maximized when $S_h = 0.5$, aligning with the JF criterion's tendency to prioritize the maximization of j . Although j reaches its peak and f is minimized when $S_z = 0$, the interaction effects among the variables adjust the optimized S_z value to 0.68. Overall, these adjustments are consistent with the conclusions from the range analysis, verifying the rationality of the optimized structural parameters.

Table 15. Comparison of structural parameters before and after optimization.

| Model | S | t_{fin} | h | d_{out} | t_{tube} | S_h | S_z | v |
|-------------------|------|-----------|-------|-----------|------------|-------|-------|-----|
| Pre-optimization | 2.2 | 0.4 | 21.5 | 27.0 | 3.5 | 8.5 | 6.0 | 1 |
| Post-optimization | 2.20 | 0.30 | 13.82 | 25.09 | 3.04 | 0.50 | 0.68 | 1 |

The performance evaluation indexes of the spiral finned tubes before and after optimization are shown in Table 16. After the optimization, the heat transfer factor j is increased by 44.44%, but the resistance factor f is increased by 14.19%. However, the increase in the resistance factor is obviously smaller than that of the heat transfer performance; thus, the comprehensive performance evaluation indicator JF is increased by 38.79%.

Table 16. Comparison of evaluation indicators before and after optimization.

| Model | j | $\Delta j/j_0$ | f | $\Delta f/f_0$ | JF | $\Delta JF/JF_0$ |
|-------------------|--------|----------------|--------|----------------|--------|------------------|
| Pre-optimization | 0.0099 | 0 | 0.0148 | 0 | 1.000 | 0 |
| Post-optimization | 0.0143 | 44.44% | 0.0169 | 14.19% | 1.3879 | 38.79% |

Using the optimized structural parameters and wind speed, Fluent simulation analysis is carried out to obtain the simulated heat transfer factor and resistance factor. Table 17 lists the predicted values of Fluent simulation and the optimized values with SVR-GA, where the error of the j factor is 2.14% and the error of the f factor is 1.2%. Small errors demonstrate the accuracy of the joint optimization method of SVR-GA.

Table 17. SVR regression model and genetic algorithm results test.

| Parameter | Predicted Value | Simulated Value | Error |
|-----------|-----------------|-----------------|-------|
| j | 0.0143 | 0.0140 | 2.14% |
| f | 0.0169 | 0.0167 | 1.2% |

6. Conclusions

Most of the current research on structural parameter optimization of the spiral finned tube heat exchanger has not fully considered the influence of internal fluid on heat transfer efficiency, and the exploration of structural parameters is not comprehensive enough. This paper adopted the fin pitch, fin thickness, fin height, base tube diameter, base tube thickness, lateral spacing, and longitudinal spacing to conduct a three-dimensional computational fluid dynamics (CFD) analysis. Through orthogonal experimental design, the specific effects of these parameters on the performance of spiral finned tube bundles were systematically evaluated. In addition, the study also focused on the effect of the Reynolds number on heat transfer performance and comprehensively evaluated the performance of the heat exchanger by combining the heat transfer performance factor j and the resistance performance factor f . With the help of support vector regression and the genetic algorithm optimization, an optimal configuration of the structural parameters of the heat exchanger was determined to achieve the balance between the factors j and f .

This study designed 47 schemes through an orthogonal experimental design with seven factors at five levels and additionally introduced wind speed as an eighth factor with three levels, expanding the total number of experiments to 147. The analysis showed that wind speed is linearly correlated with the Reynolds number. As the wind speed increases, the Nusselt coefficient and the pressure difference between the air inlet and outlet gradually increase, while the heat transfer performance factor j and the resistance performance factor f show a decreasing trend. The range analysis is used to evaluate the effect of the structural parameters on the performance of the heat exchanger. The SVR models are trained to predict the factors j and f , respectively, and j and f are combined to obtain a comprehensive evaluation indicator JF . An optimization model is constructed to optimize JF , and SVR and the GA algorithm are combined to solve the optimal structural parameters. After the optimization, j increased by 44.44%, f increased by 14.19%, and JF increased by 38.79%. The accuracy of the optimization is verified by the finite element numerical simulation developed by the optimal structural parameters.

In our future work, more factors such as the material of the spiral finned tube and the cross-sectional shape of the fins can be introduced to conduct a more comprehensive study.

Author Contributions: Resources, methodology, software, writing—original draft, H.J.; formal analysis, validation, finding acquisition, writing—reviewing and editing, T.J.; methodology, software, writing—original draft, H.T.; investigation, methodology, writing—reviewing and editing, Q.W.; conceptualization, investigation, methodology, supervision, C.D.; conceptualization, investigation, R.Z. All authors have read and agreed to the published version of the manuscript.

Funding: This research is supported by the Southwest Oil and Gas Field Innovation Fund Project (No. 2024D7-19).

Data Availability Statement: Data related to the current study are available from the corresponding author upon reasonable request.

Conflicts of Interest: Author Huaquan Jiang and Tingting Jiang were employed by the company Chongqing Xiangguosi Gas Storage limited company. Author Renliang Zhang was employed by the company Chongqing Zhizhan Gear Transmission Co., Ltd. The remaining authors declare that the research was conducted in the absence of any commercial or financial relationships that could be construed as a potential conflict of interest.

References

1. Kakac, S.; Liu, H.; Pramuanjaroenkij, A. *Heat Exchangers: Selection, Rating, and Thermal Design*; CRC Press: Boca Raton, FL, USA, 2002.
2. Yuan, M.; Zhang, W.; Liu, G.; Zhang, X.; Yousif, M.Z.; Song, J.; Lim, H. Performance study of spiral finned tubes on heat transfer and wake flow structure. *Int. J. Heat Mass Transf.* **2022**, *196*, 123278. [[CrossRef](#)]
3. Rich, D.G. *The Effect of the Number of Tube Rows on Heat Transfer Performance of Smooth Plate Fin-and-Tube Heat Exchangers*; ASHRAE Trans: Atlantic City, NJ, USA, 1975; pp. 307–319.

4. McQuiston, F.C. *Correlation for Heat, Mass and Momentum Transport Coefficients for Plate-Fin-Tube Heat Transfer Surfaces with Staggered Tube*; ASHRAE Trans: Atlantic City, NJ, USA, 1978; pp. 294–309.
5. Gray, D.; Webb, R.L. Heat transfer and friction correlations for plate finned-tube heat exchangers having plain fins. In Proceedings of the International Heat Transfer Conference Digital Library, Dubrovnik, Yugoslavia, 1–5 September 1986.
6. Nuntaphan, A.; Kiatsiriroat, T.; Wang, C.-C. Air side performance at low Reynolds number of cross-flow heat exchanger using crimped spiral fins. *Int. Commun. Heat Mass Transf.* **2005**, *32*, 151–165. [[CrossRef](#)]
7. Bhuiyan, A.A.; Amin, M.R.; Islam, A.S. Three-dimensional performance analysis of plain fin tube heat exchangers in transitional regime. *Appl. Therm. Eng.* **2013**, *50*, 445–454. [[CrossRef](#)]
8. Syuhada, A.; Afandi, D.; Sofyan, S.E. Convective heat transfer study on the spiral finned tube heat exchanger under various fin pitch arrangements. In Proceedings of the IOP Conference Series: Earth and Environmental Science, Bangkok, Thailand, 11–14 December 2019; p. 012024.
9. Keawkamrop, T.; Mesgarpour, M.; Dalkılıç, A.S.; Ahn, H.S.; Mahian, O.; Wongwises, S. Effect of the segmented fin height on the air-side performance of serrated welded spiral fin-and-tube heat exchangers. *Case Stud. Therm. Eng.* **2022**, *35*, 102128. [[CrossRef](#)]
10. Liu, L.; Cao, Z.; Shen, T.; Zhang, L.; Zhang, L. Experimental and numerical investigation on flow and heat transfer characteristics of a multi-waves internally spiral finned tube. *Int. J. Heat Mass Transf.* **2021**, *172*, 121104. [[CrossRef](#)]
11. Afandi, D.; Syuhada, A.; Sofyan, S.E. Airside Heat Transfer and Pressure Drop on the Spiral Finned-Tube Compact Heat Exchanger with Sharp Turns. In Proceedings of the 2nd International Conference on Experimental and Computational Mechanics in Engineering: ICECME 2020, Banda Aceh, Indonesia, 13–14 October 2021; pp. 53–62.
12. Mauro, G.M.; Iasiello, M.; Bianco, N.; Chiu, W.K.S.; Naso, V. Mono- and Multi-Objective CFD Optimization of Graded Foam-Filled Channels. *Materials* **2022**, *15*, 968. [[CrossRef](#)] [[PubMed](#)]
13. Bianco, N.; Fragnito, A.; Iasiello, M.; Mauro, G.M. A CFD multi-objective optimization framework to design a wall-type heat recovery and ventilation unit with phase change material. *Appl. Energy* **2023**, *347*, 121368. [[CrossRef](#)]
14. Rabienataj Darzi, A.A.; Mousavi, S.M.; Razbin, M.; Li, M. Utilizing neural networks and genetic algorithms in AI-assisted CFD for optimizing PCM-based thermal energy storage units with extended surfaces. *Therm. Sci. Eng. Prog.* **2024**, *54*, 102795. [[CrossRef](#)]
15. Park, Y.; Kim, J.; Oh, J.; Han, U.; Lee, H. Multi-objective optimization of an offset strip fin heat exchanger for waste heat recovery in electric vehicles. *Appl. Therm. Eng.* **2023**, *228*, 120533. [[CrossRef](#)]
16. Mousavi, S.M.S.; Alavi, S.M.A. Experimental and numerical study to optimize flow and heat transfer of airfoil-shaped turbulators in a double-pipe heat exchanger. *Appl. Therm. Eng.* **2022**, *215*, 118961. [[CrossRef](#)]
17. Nia, M.F.; Farzad, H.; Ansari, A.B.; Ghodrati, M.; Nassab, S.A.G.; Behnia, M. Performance improvement of a tubular heat exchanger by tube arrangement optimization using simulated annealing algorithm and blocked-off method. *Therm. Sci. Eng. Prog.* **2023**, *40*, 101793.
18. Lee, G.; Joo, Y.; Lee, S.-U.; Kim, T.; Yu, Y.; Kim, H.-G. Design optimization of heat exchanger using deep reinforcement learning. *Int. Commun. Heat Mass Transf.* **2024**, *159*, 107991. [[CrossRef](#)]
19. Cao, J.; Yuan, Y.; Zhang, Z.; Xiao, Z.; Wang, X. Variable-dimension optimization study and design of internally finned helically coiled tubes heat exchangers based on numerical simulation and experiment. *Appl. Therm. Eng.* **2024**, *248*, 123340. [[CrossRef](#)]
20. Tang, S.; Li, H.; Zhou, J.; Li, H.; Zhang, D. Parametric investigation and correlation development for thermal-hydraulic characteristics of honeycomb 4H-type finned tube heat exchangers. *Appl. Therm. Eng.* **2021**, *199*, 117542. [[CrossRef](#)]
21. Välikangas, T.; Folkersma, M.; Dal Maso, M.; Keskitalo, T.; Peltonen, P.; Vuorinen, V. Parametric CFD study for finding the optimal tube arrangement of a fin-and-tube heat exchanger with plain fins in a marine environment. *Appl. Therm. Eng.* **2022**, *200*, 117642. [[CrossRef](#)]
22. Wang, Y.; Zhao, W.; Wang, P.; Jiang, J.; Luo, X. Thermal performance of elliptical fin-and-tube heat exchangers with vortex generator under various inclination angles. *J. Therm. Sci.* **2021**, *30*, 257–270. [[CrossRef](#)]
23. Feng, Z.; Xin, C.; Zhou, T.; Zhang, J.; Fu, T. Airside thermal-hydraulic and fouling performances of economizers with integrally-molded spiral finned tubes for residual heat recovery. *Appl. Therm. Eng.* **2022**, *211*, 118365. [[CrossRef](#)]
24. Herrmann, S.; Vogel, E. Viscosity Measurements on Gaseous Methane: Re-evaluation. *Int. J. Thermophys.* **2022**, *43*, 67. [[CrossRef](#)]
25. Kays, W.M.; London, A.L. *Compact Heat Exchangers*, 3rd ed.; McGraw-Hill Book Company: New York, NY, USA, 1984.
26. Zeng, M.; Tang, L.; Lin, M.; Wang, Q. Optimization of heat exchangers with vortex-generator fin by Taguchi method. *Appl. Therm. Eng.* **2010**, *30*, 1775–1783. [[CrossRef](#)]
27. Kwon, H.; Park, S.; Choi, J.; Han, J. A Study on the Optimization of the Louver Fin Heat Exchanger for Fuel Cell Electric Vehicle Using Genetic Algorithm. *Appl. Sci.* **2023**, *13*, 2539. [[CrossRef](#)]

Disclaimer/Publisher’s Note: The statements, opinions and data contained in all publications are solely those of the individual author(s) and contributor(s) and not of MDPI and/or the editor(s). MDPI and/or the editor(s) disclaim responsibility for any injury to people or property resulting from any ideas, methods, instructions or products referred to in the content.